Applied Catalysis B: Environmental 174–175 (2015) 477–485

Contents lists available at ScienceDirect

Applied Catalysis B: Environmental

journal homepage: www.elsevier.com/locate/apcatb

Facile synthesis of porous graphene-like carbon nitride ($C_6N_9H_3$) with excellent photocatalytic activity for NO removal

Guohui Dong[a,b], Wingkei Ho[a,c,*], Yuhan Li[a], Lizhi Zhang[b]

[a] Department of Science and Environmental Studies and Centre for Education in Environmental Sustainability, The Hong Kong Institute of Education, Tai Po, N.T. Hong Kong, People's Republic of China
[b] Key Laboratory of Pesticide and Chemical Biology of Ministry of Education, College of Chemistry, Central China Normal University, Wuhan 430079, People's Republic of China
[c] Key Lab of Aerosol Chemistry & Physics, Institute of Earth Environment, Chinese Academy of Sciences, Xi'an 710075, China

ARTICLE INFO

Article history:
Received 17 February 2015
Received in revised form 19 March 2015
Accepted 23 March 2015
Available online 24 March 2015

Keywords:
Porous
$C_6N_9H_3$
Photocatalytic
NO removal
Visible light

ABSTRACT

We reported the possible synthesis of a new porous graphene-like carbon nitride ($C_6N_9H_3$) by simply adding hydrochloric acid in the precursor of block g-C_3N_4. The formation of the porous graphene-like $C_6N_9H_3$ can be attributed to the change in the thermal condensation modal of the precursor and the acidic condition induced by Cl^- and H^+. The photocatalytic activity of the samples was evaluated by the removal of NO under visible light illumination. We found that the porous graphene-like $C_6N_9H_3$ exhibited enhanced photocatalytic activity compared to the block g-C_3N_4. We also researched the removal mechanism and found that the removal of NO in our systems was due to the synergic effect of h^+ and $^{\bullet}O_2^-$. This study could shed light on the design of efficient photocatalysts and facilitate a deep understanding of the NO removal mechanism through photocatalytic technology.

1. Introduction

Since the evolution of oxygen and hydrogen at a semiconductor electrode under light irradiation was discovered by Fujishima and Honda in 1972 [1], the technology of semiconductor photocatalysis has attracted global interest because of its potential applications in water splitting, environmental cleanup, conversion of solar energy, and organic synthesis [2–6]. In 2009, Wang, et al. reported that a metal-free polymer semiconductor, graphitic carbon nitride (g-C_3N_4) with an optical band gap of 2.7 eV, could produce hydrogen or oxygen by splitting water under visible light irradiation [7]. Besides having a suitable band gap energy, this material can withstand acids, alkalis, and high temperature because of the strong covalent bonds between carbon and nitride atoms. As such, this material has attracted considerable attention from numerous researchers. However, block g-C_3N_4 suffers from low photoreactivity, which is caused by the fast recombination of photogenerated electrons and holes [8]. Therefore, numerous efforts have been focused on improving the photocatalytic performance of carbon nitride polymer semiconductors. For example, doping with foreign elements [9–11], self-doping with carbon elements [12], coupling with metals or other semiconductors [13–15], copolymerization [16–18], introducing formate anion or iodide ions [19,20], and oxidation with H_2O_2 were found to improve the photoreactivity of g-C_3N_4 [21]. Besides these methods, the photoreactivity of g-C_3N_4 is also affected by its morphology [22,23], which is typically related to the material's surface properties, such as surface structure and surface area [24]. Thus, creating a special morphology presents another important method to enhance the photocatalytic activity of g-C_3N_4. For instance, one-dimensional carbon nitride nanostructures, such as nanotubes and nanofibers, have displayed enhanced photocatalytic activity in comparison with block g-C_3N_4 because of its fast photoresponse [25,26]. Porosification could significantly enhance the photoreactivity of g-C_3N_4 because of the larger number of surface active sites [27,28]. Hollow carbon nitride nanospheres improved H_2 evolution activity over that of bulk g-C_3N_4 [29]. The improvement could be attributed to the inner optical reflection and improved structure condensation. Nanosheets have been proven advantageous for promoting the photocatalytic efficiency of g-C_3N_4 [30,31]. However, the activities of these kinds of nanostructure carbon nitride are still moderate, which means that the current nanostructures cannot fulfill the photocatalytic properties of graphitic carbon nitride. Thus, new special nanostructure

* Corresponding author at: Department of Science and Environmental Studies and Centre for Education in Environmental Sustainability, The Hong Kong Institute of Education, Tai Po, N.T. Hong Kong, People's Republic of China.
Tel.: +852 2948 8255.
E-mail address: keithho@ied.edu.hk (W. Ho).

http://dx.doi.org/10.1016/j.apcatb.2015.03.035
0926-3373/

carbon nitride with high photocatalytic activity should be designed and developed.

Recently, Wang and co-workers reported a new kind of nanospherical carbon nitride composed of g-C_3N_4 nanosheets [23]. Synergism between the nanosheets and nanosphere in the complex nanoarchitectures could significantly enhance the photocatalytic H_2 evolution performance of g-C_3N_4. This design idea of carbon nitride nanostructure provides a significant direction for researchers. Given that synergism exists between the nanosheets and the nanosphere, we suppose that a similar synergism may also exist between the nanosheets and nanopores. We therefore believe that the combination of nanopores with nanosheets could generate a new kind of photocatalytic system, which has never been reported previously and should present a challenging endeavor of general interest in numerous fields.

In this study, we synthesized a new porous graphene-like carbon nitride: $C_6N_9H_3$. Moreover, this new porous graphene-like $C_6N_9H_3$ exhibited enhanced photocatalytic activity compared with the block g-C_3N_4 in terms of nitrous oxide (NO) removal under visible light illumination. A series of experiments are designed to clarify the formation mechanism of porous graphene-like $C_6N_9H_3$. The reasons for the excellent photocatalytic activity of $C_6N_9H_3$ for the removal of NO are analyzed in detail.

2. Experimental

2.1. Synthesis of carbon nitride photocatalysts

All chemicals were analytical-grade reagents and used without further purification. In a typical procedure, melamine (2,4,6-triamino-*s*-triazine, $C_3N_3(NH_2)_3$) was first dissolved in 80 mL of hot distilled water. After cooling, different amounts of hydrochloric acid (HCl) (37%) were then slowly added into the melamine solution with magnetic stirring. After 30 min, the solution was transferred to an oven to thoroughly evaporate the water at 120 °C. The resulting solid was placed in a covered crucible and then heated to 500 °C in a muffle furnace for 2 h with a heating rate of 20 °C/min followed by further heat treatment at 520 °C for 2 h. The final samples prepared by adding concentrated HCl (37%) solution at 0, 0.5, 1, and 1.5 mL were respectively denoted as HA0-CN, HA0.5-CN, HA1.0-CN, and HA1.5-CN. Note that the reproducibility of the synthesis method was excellent.

2.2. Characterization

The powder X-ray diffraction (XRD) patterns were recorded using a Bruker D8 Advance diffractometer with monochromatized Cu Kα radiation (λ = 1.5418 Å). Transmission electron microscopy (TEM) images were obtained using a JEOL JSM-2010 microscope with an accelerating voltage of 200 kV. The TEM samples were prepared by dispersing the final powders in ethanol, and the dispersion was then placed on lacey support film grids. The weight ratio of each element in different samples was determined via elemental analysis (EA, Vario EL III CHNSO). XPS measurements were obtained using a VG scientific ESCALAB Mark II spectrometer equipped with two ultra-high vacuum chambers. All binding energies were calibrated to the C 1s peak at 284.6 eV of the surface adventitious carbon. The nitrogen adsorption and desorption isotherms at 77 K were measured using Micrometrics ASAP2020 system after the samples were vacuum-dried at 180 °C overnight. UV–vis diffuse reflectance spectra (DRS) were obtained using a UV–vis spectrometer (Shimadzu UV-3600) with $BaSO_4$ as a reference and were converted from reflection to absorbance via the Kubelka–Munk method. The photoluminescence spectra (PL) of the samples were obtained using a fluorescence spectrometer (Hitachi F-4500) at 293 K.

Photocurrent experiments were performed in a conventional three-electrode cell with a platinum plate (1 cm × 1 cm) as the auxiliary electrode and a saturated calomel electrode as the reference electrode on a CHI 660C workstation. The photoelectrode (photoelectrodes consisted of different samples) was positioned in the middle of a 0.1 M KCl aqueous solution with the glass side facing the incident light. A 300 W Xe lamp with a 420 nm cutoff filter was selected as the visible light source.

2.3. Photocatalytic activity test

The photocatalytic activity experiments on the resulting samples for NO removal at ppb levels were performed at ambient temperature in a continuous flow reactor. The volume of the rectangular reactor, which was made up of stainless steel and covered with quartz glass, was 4.5 L (30 cm × 15 cm × 10 cm [L × W × H]). One sample dish containing the photocatalysts was placed in the middle of the reactor. An LED lamp (λ = 448 nm, 14 W m^{-2}) was used as the simulated solar light source. The lamp was vertically placed outside the reactor above the sample dish.

Each photocatalyst sample was prepared by coating an aqueous suspension of the sample onto a dish. Typically, 0.15 g of the photocatalysts were added into 15 mL of H_2O and ultrasonicated for 20 min. The aqueous suspension was then coated onto a glass dish with a diameter of 12 cm. The coated dish was pretreated at 60 °C until water was completely removed in the suspension and then cooled to room temperature prior to photocatalytic testing.

The NO gas was obtained from a compressed gas cylinder at a concentration of 50 ppm NO (N_2 balance, BOC gas) with traceable National Institute of Stands and Technology (NIST) standard. The initial concentration of NO was diluted to about 600 ppb by the air stream supplied by a zero air generator. The gas streams were completely premixed by a gas blender, and the flow rate was controlled at 1 L/min by a mass flow controller. After adsorption–desorption equilibrium among gases and photocatalysts was achieved, the lamp was turned on. The concentration of NO was continuously measured using a chemiluminescence NO analyzer. The removal efficiency (η) of NO was calculated as follows:

$$\eta(\%) = (1 - C/C_0) \times 100\%$$

where C and C_0 are the concentrations of NO in the outlet steam and the feeding stream, respectively.

The quantum efficiency (%) of each sample was calculated as follow:

$$\text{Quantum efficiency}(\%) = (n \times \text{mole of reduction products/moles of photon flux input}) \times 100\%$$

where n is the number of moles of holes required to produce one mole of oxidation product from NO.

3. Results and discussion

3.1. Structural characterization of result samples

X-ray diffraction was performed to characterize the phase structure of the products. Fig. 1 shows the powder XRD patterns of the as-prepared samples. From these patterns, two peaks are found in all samples. These two peaks at 13° and 27.41° match well with the (1 0 0) and (0 0 2) crystal planes of graphitic carbon nitride. This result demonstrates that the synthesized samples were graphitic carbon nitride. The small angle peak at 13°, which corresponds to 0.676 nm, is due to the in-plane structural packing motif. The strong peak at 27.41° is a characteristic interlayer stacking peak and corresponds to an interlayer distance of d = 0.336 nm. However, the peaks

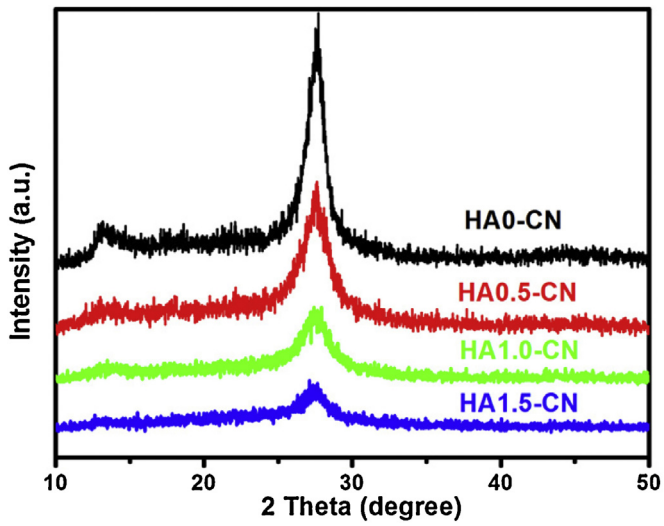

Fig. 1. XRD patterns of HA0-CN, HA0.5-CN, HA1.0-CN, and HA1.5-CN samples.

at 27.41° of HA0.5-CN, HA1.0-CN, and HA1.5-CN became weaker and broader than that of HA0-CN, which was mainly caused by the destruction of the interlayer structure. This result implied that the block structure may be changed into ultrathin nanosheet structure.

The microstructures of the resulting samples were investigated via transmission electron microscopy (TEM). Fig. 2 shows the variation in carbon nitride morphologies with increasing HCl amount in the synthesis process. Without HCl in the synthesis process, the morphol-ogy of HA0-CN was of a block-like structure, and no porosity can be observed on the sample (Fig. 2a). Increasing the HCl amount to 0.5 mL yielded a similar block-like structure of HA0.5-CN, but a porous texture could be observed in the image (Fig. 2b). When we increased the amount of HCl from 0.5 mL to 1.0 mL, the HA1.0-CN sample was composed of porous ultrathin nanosheets with a thickness of 10 nm (Fig. 2c). This observation corresponds well with the XRD results, and suggests that the porous graphene-like carbon nitride has been successfully synthesized. However, when the amount of HCl was further increased to 1.5 mL, the sizes of the pores increased. Meanwhile, the nanosheets were broken into fragments (Fig. 2d). From these phenomena, we can conclude that the HCl content in the precursor will change the block structure into a porous thin layer structure, and varying the amount of HCl corresponds to different pore sizes and different numbers of layers.

Elemental analysis was used to determine the molar ratio of C, N, and H in block carbon nitride (HA0-CN) and porous graphene-like carbon nitride (HA1.0-CN). The resulting ratio for HA0-CN was 3:4:0, which is consistent with the theoretical value (C_3N_4). Surprisingly, a different result (6:9:3) was got from the detection of HA1.0-CN, meaning that a new kind of porous graphene-like carbon nitride ($C_6N_9H_3$) can be synthesized by simply modifying the precursor of block g-C_3N_4.

3.2. Formation mechanism of porous graphene-like $C_6N_9H_3$

To clarify the formation mechanism of porous graphene-like $C_6N_9H_3$ (HA1.0-CN), the weight ratios of C, N, Cl, and H of the precursor of HA1.0-CN were determined via elemental analysis. The contents of C, N, H, and Cl are 21%, 54.64%, 4.4%, and 19.96%,

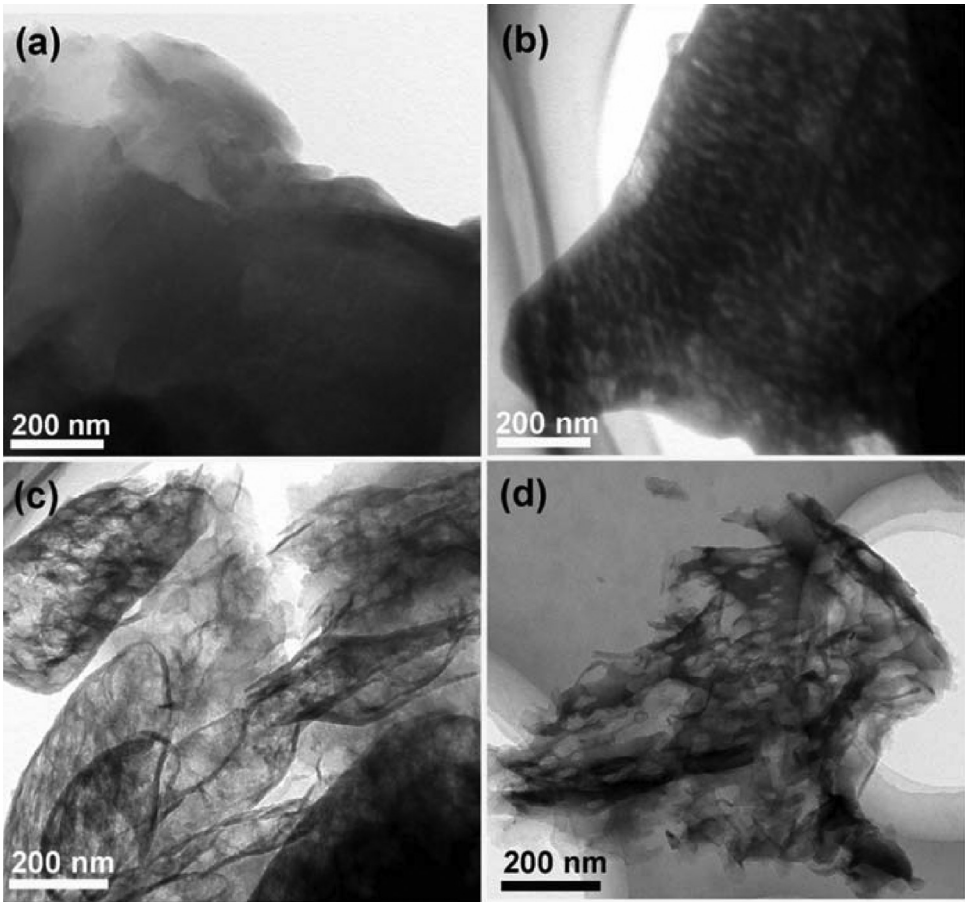

Fig. 2. TEM images of HA0-CN (a); HA0.5-CN (b); HA1.0-CN (c); and HA1.5-CN (d) samples.

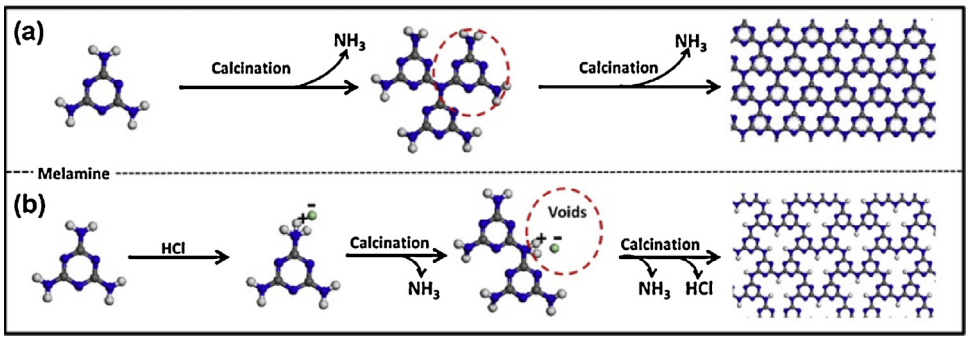

Fig. 3. The thermal condensation process of melamine in the absence (a) or presence of HCl (b).

respectively. Therefore, the molecular formula of the precursor is $C_3N_6H_6$•HCl, suggesting that part of the amino groups of melamine ($C_3N_6H_6$) reacted with HCl and produced an ammonium salt ($C_3N_6H_6$•HCl) like NH_4Cl. We think that HCl will change the condensation modal of melamine and induce the formation of porous graphene-like $C_6N_9H_3$. This is because the amino groups which reacted with HCl may incompletely participate in the subsequent thermal condensation due to the protection of HCl. In that case, a large number of voids (pores) would be formed around those amino groups (Fig. 3). In the meantime, bridging nitrogens in HA1.0-CN will be changed from three-coordinated bridging nitrogens to two-coordinated bridging nitrogens (Fig. 3). To test this hypothesis, X-ray photoelectron spectroscopy (XPS) was performed to investigate the chemical compositions of HA0-CN and HA1.0-CN. The survey spectra and the high-resolution Cl 2p spectra proved that the resulting samples did not contain Cl (Fig. 4a and b). We therefore believe that HCl was released in the calcination process (This will be discussed later). From Fig. 4c, the C 1s spectrum of HA1.0-CN is similar to that of HA0-CN, which means that the chemical structure of C in HA1.0-CN is the same as that in HA0-CN. In the N 1s spectra (Fig. 4d), the peak at 398.4 eV could be attributed to the C—N—C groups, whereas the peak at 400.7 eV originated from the tertiary nitrogen N—$(C)_3$ groups [8,27]. Notably, the peak at 400.6 eV disappeared from the N 1s spectra of HA1.0-CN. Meanwhile, a new peak at 401.3 eV, which could be attributed to H—N—$(C)_2$ [32,33], appeared in the N 1s spectra of HA1.0-CN. These changes confirm that the triazine rings in HA1.0-CN are mainly connected through two-coordinated bridging nitrogens. A similar porous CN structure was reported in a previous literature reported by Deifallah [34]. In their literature, the molecular formula of the CN structure which combined with two-coordinated bridging nitrogens could be written as $C_6N_9H_3$. However, the synthetic method of $C_6N_9H_3$ in their report is very complex. Based on above analysis and experiments, we conclude that the formation of $C_6N_9H_3$ in our system can be

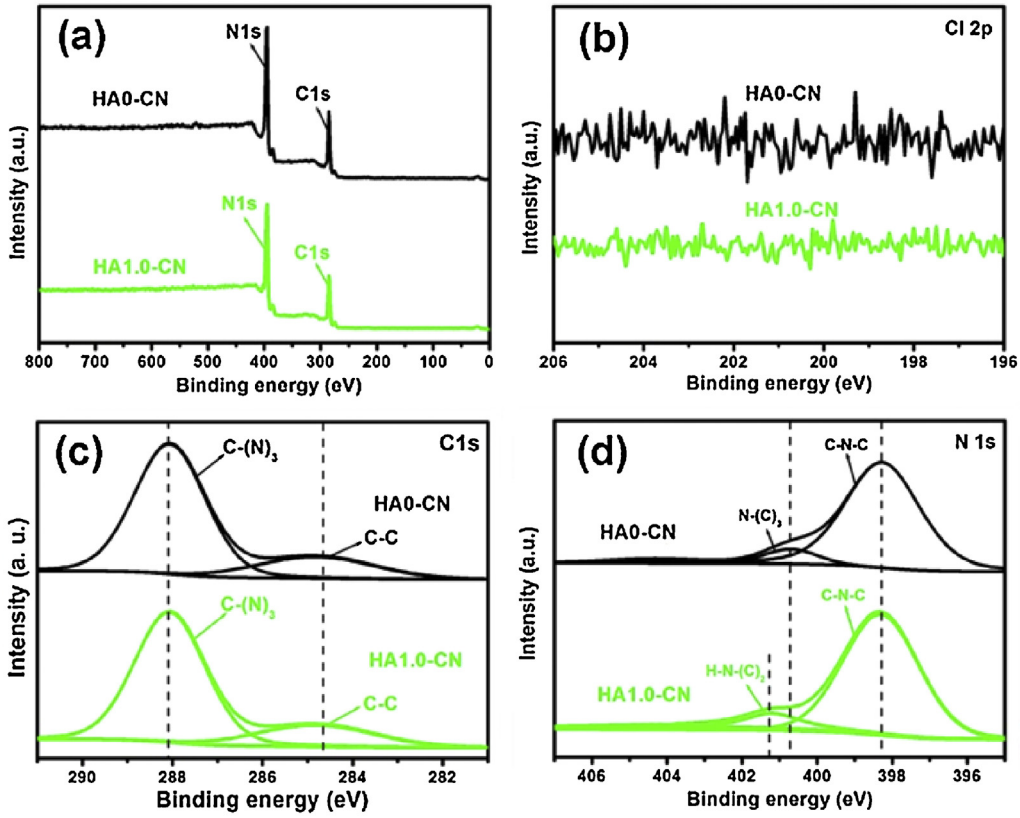

Fig. 4. XPS spectra of the resulting samples: (a) survey of the sample HA0-CN and HA1.0-CN; (b) the high-resolution Cl 2p spectra of HA0-CN and HA1.0-CN; (c) the high-resolution C 1s spectra of HA0-CN and HA1.0-CN; and (d) the high-resolution N 1s spectra of HA0-CN and HA1.0-CN.

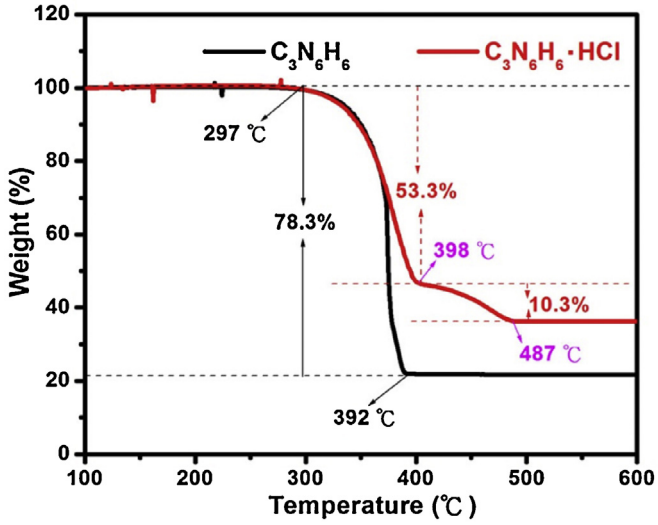

Fig. 5. TGA curves of melamine ($C_3N_6H_6$) and precursor of HA1.0-CN ($C_3N_6H_6$•HCl).

attributed to the change in the thermal condensation modal of melamine induced by HCl.

In order to know when the HCl released from $C_6N_9H_3$, thermogravimetric analysis (TGA) was used to measure changes in the weight of melamine ($C_3N_6H_6$) and precursor of HA1.0-CN ($C_3N_6H_6$•HCl) as a function of temperature. It can be seen from Fig. 5 that during calcination under argon atmosphere both $C_3N_6H_6$ and $C_3N_6H_6$•HCl show the sharp mass loss in the temperature range of about 297–392 °C, which could be attributed to the thermal condensation of melamine to form carbon nitride and NH_3. However, the mass loss of the precursor of $C_3N_6H_6$•HCl less than that of $C_3N_6H_6$, suggesting that the amount of released NH_3 in the thermal condensation of $C_3N_6H_6$•HCl less than that of $C_3N_6H_6$. This further confirmed that HCl changed the condensation modal of melamine and induced the formation $C_6N_9H_3$. More importantly, another mass loss in the temperature range of about 398–487 °C could be observed for $C_3N_6H_6$•HCl but not for $C_3N_6H_6$, implying that HCl could be released after changing the condensation modal of melamine. This is consistent with the result of XPS.

To further clear the formation mechanism of porous graphene-like $C_6N_9H_3$, we investigated the influences of H^+ and Cl^- in the growth processes. We first used HNO_3 instead of HCl to study the morphology of the resulting sample. When Cl^- was replaced by NO_3^- while maintaining the same acidity as that for synthesizing HA1.0-CN, the morphology of the as-prepared sample NA-CN was that of ultrathin nanosheets (Fig. 6b). Notably, however, no pores could be observed in the image of NA-CN. To discount the influence of NO_3^-, we prepared the control sample (NS-CN) at the same conditions as that for sample NA-CN, but $NaNO_3$ was used to replace HNO_3. Fig. 6c shows that the morphology of NS-CN was a block-like structure. Therefore, we can conclude that acidic conditions are favorable for the formation of carbon nitride nanosheets. Given that an acidic condition is only favorable for the formation of carbon nitride nanosheets, logically, the chloride ion may induce the formation of porous carbon nitride. To test this inference, we prepared another control sample (SC-CN) at the same condition as that for sample HA1.0-CN, but NaCl was used to replace HCl. Fig. 6d shows that the morphology of SC-CN was a porous block structure, thereby confirming that the chloride ion can lead to the formation of porous carbon nitride.

From the above analysis, the possible formation mechanism of porous graphene-like $C_6N_9H_3$ can be proposed as follows: melamine first reacted with HCl and formed a new precursor ($C_3N_6H_6$•HCl). On one hand, the amino groups were partly protected by HCl. This protection changed the modal of thermal condensation and induced the formation of the porous $C_6N_9H_3$. On

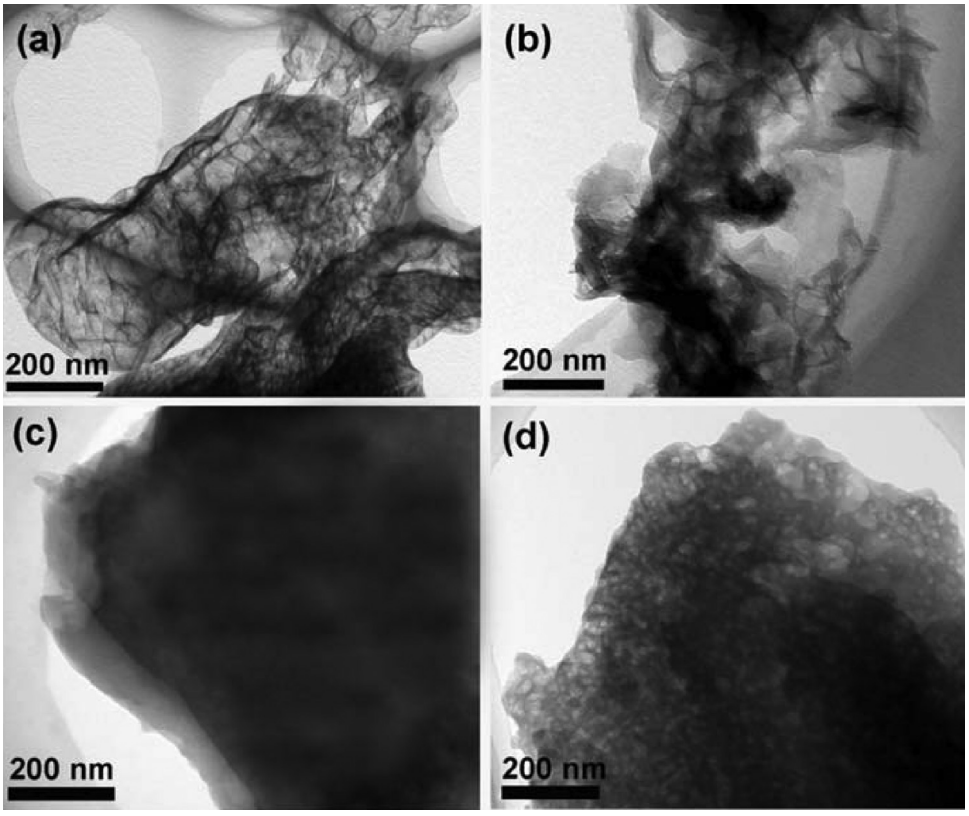

Fig. 6. TEM images of HA1.0-CN (a); NA-CN (b); SN-CN (c); and SC-CN (d) samples.

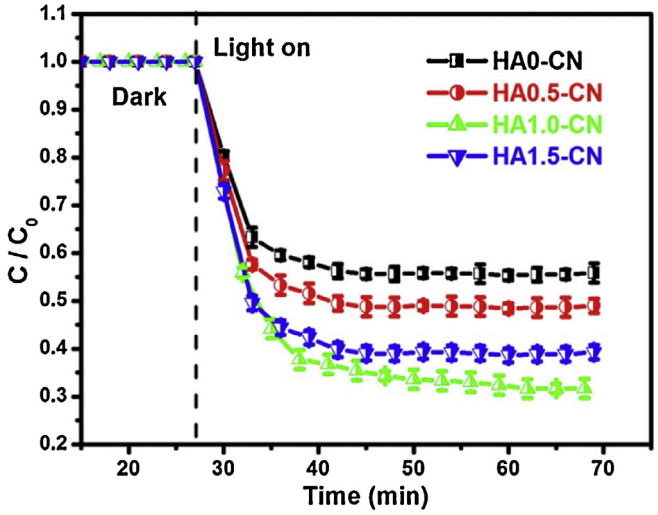

Fig. 7. Comparison of the photocatalytic removal of NO in the presence HA0-CN, HA0.5-CN, HA1.0-CN, and HA1.5-CN samples.

the other hand, the acidic condition, which was provided by HCl, simultaneously induced the formation of $C_6N_9H_3$ nanosheet.

3.3. Photocatalytic activities

NO is a representative indoor air pollutant that originates from furnishings and decorating materials. This gas presents significant health effects, such as causing various health problems like neural disease. Therefore, removing indoor NO as well as increasing public awareness of its effect on the environment and health are crucial. Herein, the resulting samples were used to photocatalytically remove NO in air. Prior to visible light irradiation, the adsorption/desorption equilibrium between the gas and the photocatalysts was reached. The lamp was then turned on to initiate the photocatalytic removal of NO on the photocatalysts. Fig. 7 displays the NO concentration changes (C/C_0) versus irradiation time in the presence of the different samples. As seen from the figure, NO could not be removed via direct photolysis under visible light irradiation without the presence of any photocatalysts. However, after 40 min of visible light irradiation, the NO removal efficiency reached 43.2%, 54.3%, 71.2%, and 60.2% for HA0-CN, HA0.5-CN, HA1.0-CN, and HA1.5-CN, respectively. The concentration change of NO followed the first-order kinetics, and the removal rate of NO over HA0-CN, HA0.5-CN, HA1.0-CN, and HA1.5-CN were 0.07, 0.08, 0.14, and 0.09 min^{-1}, respectively. The quantum efficiency of HA0-CN, HA0.5-CN, HA1.0-CN, and HA1.5-CN were 0.5%, 0.6%, 0.8%, and 0.7%, respectively. With increasing amount of HCl in the synthetic process, the photocatalytic activity of carbon nitride nanostructures initially increased and then decreased. Porous graphene-like $C_6N_9H_3$ (HA1.0-CN) evidently exhibited the best photocatalytic activity on NO removal.

3.4. Activity enhancement mechanism

In general, the photocatalytic activity of a photocatalyst is primarily determined by two factors. The first factor is the surface area. A large surface area provides more surface sites for the adsorption of reactant molecules, thereby making the photocatalytic process more efficient. Therefore, nitrogen sorption was used to measure the surface areas of the resulting samples. From Fig. 8a, the Brunauer–Emmett–Teller specific surface areas are 8.5, 32.0, 345.0, and 75.0 $m^2\ g^{-1}$ for HA0-CN, HA0.5-CN, HA1.0-CN, and HA1.5-CN, respectively. Additionally, Barret–Joyner–Halenda (BJH) analysis showed that the content of HCl in precursor will convert the block structure into a porous structure (Fig. 8b). The porous graphene-like $C_6N_9H_3$ (HA1.0-CN) displayed the biggest surface area and pore volume, which is consistent with the photocatalytic activity results. Therefore, the higher surface area would contribute to the higher photocatalytic activity of the porous graphene $C_6N_9H_3$.

Aside from surface area, the second factor is the separation and recombination rates of the photogenerated electrons and holes in the photocatalysts. This factor conventionally relates to semiconductor photoexcitation, recombination of photoinduced charge carriers, and the transfer of photoinduced charge carriers. Semiconductor photoexcitation strongly depends on the photoabsorption ability and the band gap of the photocatalyst. We measured the UV–vis absorption spectra of the resulting samples and found that the absorption edges of these samples vary (Fig. 9a). All the UV–vis absorption edges of HA0.5-CN, HA1.0-CN, and HA1.5-CN showed a blue shift compared with that of HA0-CN. This occurrence is indicative of the quantum confinement effect (QCE), which is caused by porosification and exfoliation in our system. The band gaps optically obtained were approximately 2.70, 2.76, 2.83, and 2.79 eV for the samples of HA0.5-CN, HA1.0-CN, and HA1.5-CN, respectively (Fig. 9b). QCE is known to invariably increase the intrinsic bandgap by oppositely shifting the valence and conduction band edges. Besides providing more powerful photogenerated holes and electrons, QCE also inhibits the recombination of the photogenerated electrons and holes. Moreover, as a result of the delamination effect, the charge migration distance from bulk to the surface was remarkably reduced, and thus reducing their recombination possibility during their migration [28,30,31]. To test this deduction, we performed PL measurements to study the separation of photogenerated electrons and holes in different samples. Fig. 9c

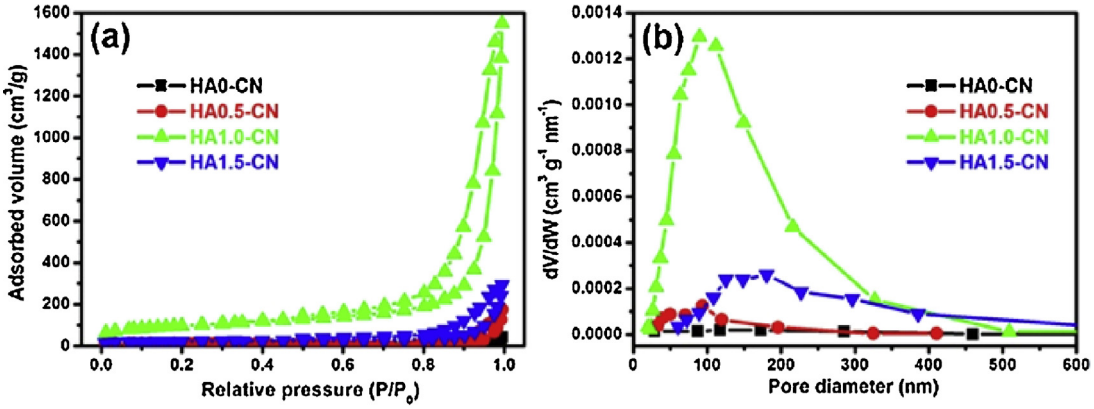

Fig. 8. N_2 adsorption–desorption isotherms (a) and BJH pore size distribution plots (b) of HA0-CN, HA0.5-CN, HA1.0-CN, and HA1.5-CN samples.

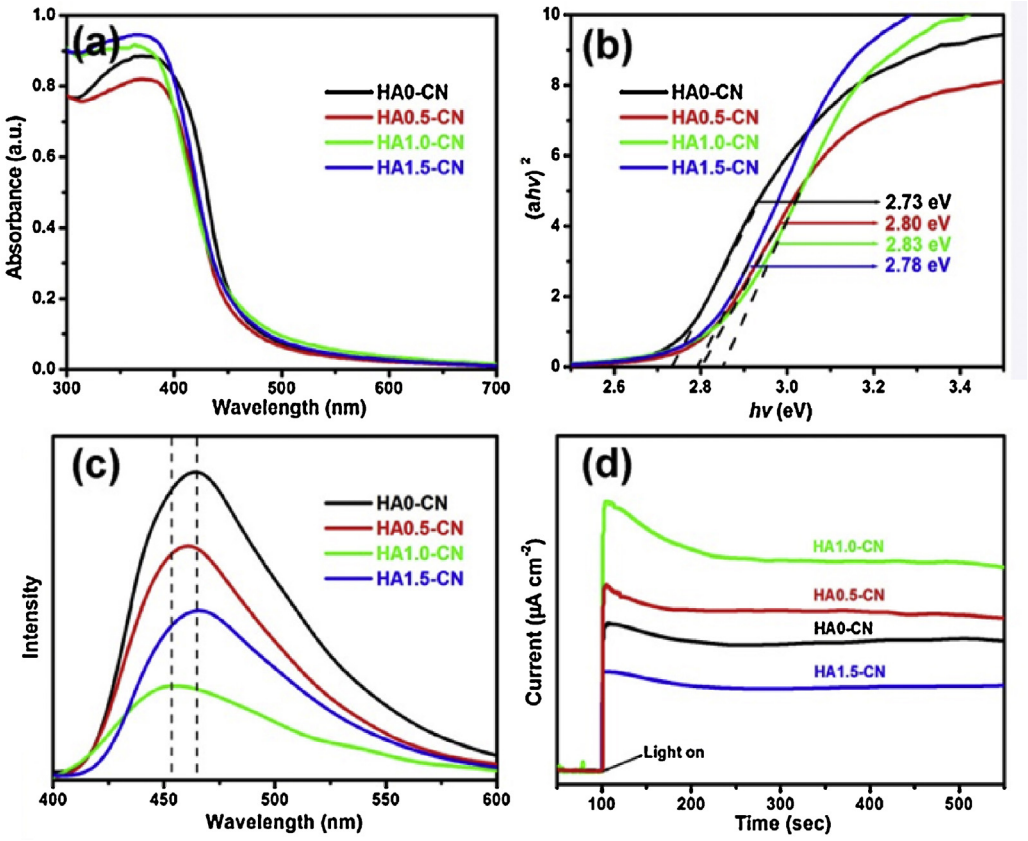

Fig. 9. UV–vis absorption spectra (a), transformed diffuse reflectance spectra (b) PL spectra (c) and Current-time curves (d) of HA0-CN, HA0.5-CN, HA1.0-CN, and HA1.5-CN samples.

displays the PL spectra of the samples under excitation at 330 nm and at room temperature. The strong emission peak of HA0-CN around 455 nm is derived from the direct electron and hole recombination of band transition. HA0.5-CN, HA1.0-CN, and HA1.5-CN showed lower PL intensity compared with that of HA0-CN, which suggests their higher separation and transfer efficiency of photogenerated carriers. More importantly, porous graphene-like $C_6N_9H_3$ shows the weakest PL peak, which indicates the best promotion effect of porous graphene-like structure on the separation of the photogenerated holes and electrons. This effect can be further confirmed by the photocurrent spectra. As seen in Fig. 9d, porous graphene-like $C_6N_9H_3$ shows a higher current density than the other samples, which confirms that the porous graphene-like structure has the best charge separation efficiency.

Therefore, the best NO photocatalytic removal activity of porous graphene-like $C_6N_9H_3$ could be attributed to the high surface area induced by the porous graphene-like structure and good charge separation efficiency because of QCE and its special morphology.

3.5. The mechanism of NO removal

The photocatalytic decomposition of NO is crucial in practical applications. Therefore, an increasing number of works on the photocatalytic removal of NO have been reported in recent years. However, until now, no systematic study about the mechanism of the NO removal via the photocatalytic technique exists in the literature. Generally, the photocatalytic removal of various pollutants are attributed to photogenerated holes and electrons as well as several active oxygen species, including the superoxide ($^{\bullet}O_2^-$), hydrogen peroxide (H_2O_2), and hydroxyl radicals ($^{\bullet}OH$). We suppose that the photocatalytic removal mechanism of NO may be similar with those of other pollutants, but the active species that have significant functions in the process of NO removal requires further research.

To investigate the possible photocatalytic removal mechanism of NO over porous graphene-like $C_6N_9H_3$ (HA1.0-CN) and block g-C_3N_4 (HA0-g-C_3N_4), several experiments were carried out. First, potassium iodide (KI) and potassium dichromate ($K_2Cr_2O_7$) were used to trap photogenerated holes and electrons, respectively. As shown in Fig. 10, the rate of NO removal acutely decreased when KI or $K_2Cr_2O_7$ was added. This result suggests that both hole (h^+) and electrons (e^-) factors majorly in the photocatalytic removal process of NO, both on the porous graphene-like $C_6N_9H_3$ and block g-C_3N_4. Photogenerated electrons are known to possibly reduce oxygen to active oxygen species. Moreover, considering that the major product in our systems is NO_2 (Fig. 10c), we suppose that at least one kind of active oxygen species may have a crucial function in the NO removal process. To test this hypothesis, scavengers such as *p*-benzoquinone (PBQ) for $^{\bullet}O_2^-$ and *tert*-butyl alcohol (TBA) for $^{\bullet}OH$ were employed in the photocatalytic process of HA1.0-CN (Fig.10a) and HA0-CN (Fig. 10b). From Fig. 10a and b, no rate change was observed for the removal of NO in the presence of TBA, and no removal of NO was observed during light irradiation of the H_2O_2 and NO without photocatalysts, either on HA1.0-CN or HA0-CN. This result indicates that $^{\bullet}OH$ and H_2O_2 were ineffective in the photocatalytic removal of NO. However, the photocatalytic removal efficiencies of NO both on porous graphene-like $C_6N_9H_3$ and block g-C_3N_4 were significantly reduced with the addition of $^{\bullet}O_2^-$ scavenger PBQ, which indicates that $^{\bullet}O_2^-$ radicals factor prominently on the removal of NO. As a result, h^+ and $^{\bullet}O_2^-$ have major functions in the removal process of NO both on porous graphene-like $C_6N_9H_3$ and block g-C_3N_4. In spite of this hypothesis, the rate for

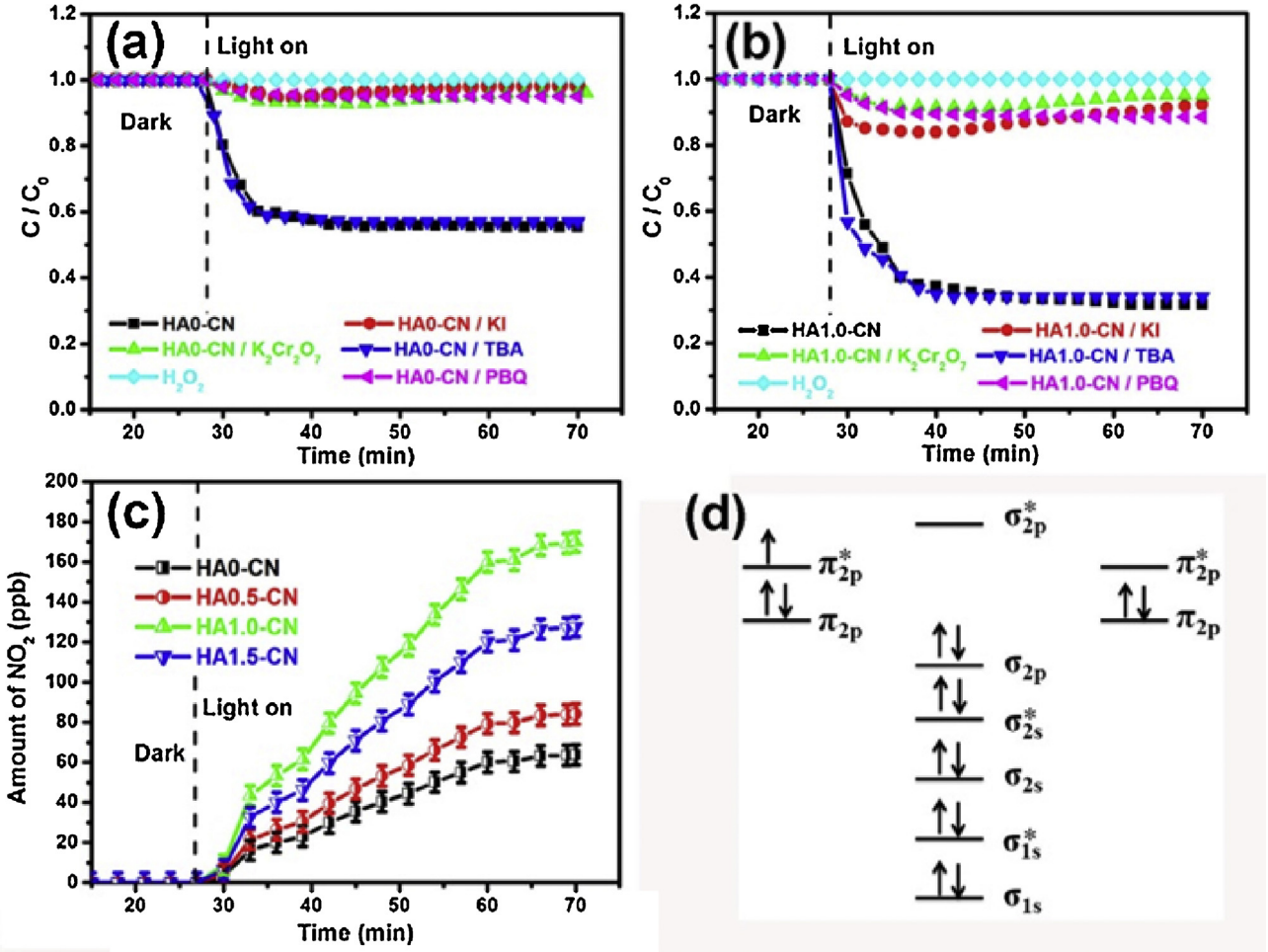

Fig. 10. Comparison of photocatalytic activities of HA0-CN in different photocatalysis systems under visible light irradiation (a); comparison of photocatalytic activities of HA1.0-CN in different photocatalysis systems under visible light irradiation (b); NO_2 generation over different samples (c); the molecular orbital diagram of NO (d).

NO removal is acutely decreased when h^+ and $^\bullet O_2^-$ solely exist. Therefore, we think that the synergic effect of h^+ and $^\bullet O_2^-$ occurs in the photocatalytic removal process of NO.

To further clarify the removal process of NO and the synergic effect between h^+ and $^\bullet O_2^-$, we analyzed the molecular orbital diagram of NO (Fig. 10d). The unpaired electron of antibonding orbital $\pi 2p^*$ can easily be taken away, which means that NO can be easily oxidized to nitrosyl cation (NO^+). Therefore, in our systems, NO may initially be oxidized to NO^+ by h^+ because the intimate contact between the absorbed NO and the surface of photocatalyst. NO^+ can then further react with $^\bullet O_2^-$ to produce NO_2·NO_2 will react with water molecules to produce nitric acid and nitrous acid. [35] Based on the above results and analyses, the removal of NO on both porous graphene-like $C_6N_9H_3$ and block g-C_3N_4 proceeds as follows:

$$\text{Carbonnitride} + \text{visiblelight} \rightarrow h^+ + e^- \quad (1)$$

$$e^- + O_2 \rightarrow {}^\bullet O_2^- \quad (2)$$

$$h^+ + NO \rightarrow NO^+ \quad (3)$$

$$2NO^+ + 2{}^\bullet O_2^- \rightarrow 2NO_2 + O_2 \quad (4)$$

$$2NO_2 + H_2O \rightarrow HNO_3 + HNO_2 \quad (5)$$

4. Conclusions

In this study, we demonstrated an easy method of fabricating new kind of porous graphene-like carbon nitride $C_6N_9H_3$. We can easily tune the morphology and crystal structure of the resulting carbon nitride by changing the amount of hydrochloric acid in the precursor. The study on the mechanism of porous graphene-like $C_6N_9H_3$ formation showed that porous graphene-like $C_6N_9H_3$ formation can be attributed to the change in the thermal condensation modal of melamine and the acidic condition induced by Cl^- and H^+, respectively. Furthermore, the increase in the surface area and quantum confinement effect, which are attributed to the special morphology, enhanced the photocatalytic activity on the removal of NO under visible light irradiation. We also researched the removal mechanism and found that the removal of NO was due to the synergic effect of h^+ and $^\bullet O_2^-$. In removal process, NO is initially oxidized to NO^+ by h^+. NO^+ then further reacts with $^\bullet O_2^-$ to produce NO_2. The new findings could shed light on the design of efficient photocatalysts and facilitate a deep understanding of the NO removal mechanism through photocatalytic technology.

Acknowledgments

This research is financially supported by the research grant of Early Career Scheme (ECS 809813) from the Research Grant Council, Hong Kong SAR Government, Dean's Research Fund-Early Career Researchers (04022), Research Equipment Grant (REG-2),

and Internal Research Grant (R3429) from The Hong Kong Institute of Education.

References

[1] A. Fujishima, K. Honda, Nature 238 (1972) 37–38.
[2] M.R. Hoffmann, S.T. Martin, W. Choi, D.W. Bahnemann, Chem. Rev. 95 (1995) 69–96.
[3] E.R. Carraway, A.J. Hoffman, M.R. Hoffmann, Environ. Sci. Technol. 28 (1994) 786–793.
[4] Y.I. Kim, S. Salim, M.J. Huq, T.E. Mallouk, J. Am. Chem. Soc. 113 (1991) 9561–9563.
[5] K. Maeda, T. Takata, M. Hara, N. Saito, Y. Inoue, H. Kobayashi, K. Domen, J. Am. Chem. Soc. 127 (2005) 8286–8287.
[6] F. Wang, C.H. Li, H.J. Chen, R.B. Jiang, L.D. Sun, Q. Li, J.F. Wang, J.C. Yu, C.H. Yan, J. Am. Chem. Soc. 135 (2013) 5588–5601.
[7] X.C. Wang, K. Maeda, A. Thomas, K. Takanabe, G. Xin, J.M. Carlsson, K. Domen, M. Antonietti, Nat. Mater. 8 (2009) 76–80.
[8] J.G. Yu, S.H. Wang, J.Q. Low, W. Xiao, Phys. Chem. Chem. Phys. 15 (2013) 16883–16890.
[9] S.C. Yan, Z.S. Li, Z.G. Zou, Langmuir 26 (2010) 3894–3910.
[10] G. Liu, P. Niu, C.H. Sun, S.C. Smith, Z.G. Chen, G.Q. Lu, H.M. Cheng, J. Am. Chem. Soc. 132 (2010) 11642–11648.
[11] Z.Z. Lin, X.C. Wang, Angew. Chem. Int. Ed. 52 (2013) 1735–1738.
[12] G.H. Dong, K. Zhao, L.Z. Zhang, Chem. Commun. 48 (2012) 6178–6180.
[13] Z.X. Ding, X.F. Chen, A. Markus, X.C. Wang, ChemSusChem 4 (2011) 274–281.
[14] C.S. Pan, J. Xu, Y.J. Wang, D. Li, Y.F. Zhu, Adv. Funct. Mater. 22 (2012) 1518–1524.
[15] J.S. Zhang, M.W. Zhang, R.Q. Sun, X.C. Wang, Angew. Chem. Int. Ed. 51 (2012) 10145–10149.
[16] J.S. Zhang, X.F. Chen, K. Takanabe, K. Maeda, K. Domen, J.D. Epping, X.Z. Fu, A. Markus, X.C. Wang, Angew. Chem. 122 (2010) 451–454.
[17] J.S. Zhang, G.G. Zhang, X.F. Chen, S. Lin, L.M. Öhlmann, G. Dolega, G. Lipner, A. Markus, S. Blechert, X.C. Wang, Angew. Chem. Int. Ed. 51 (2012) 3183–3187.
[18] Y.J. Cui, Z.X. Ding, X.Z. Fu, X.C. Wang, Angew. Chem. Int. Ed. 51 (2012) 11814–11818.
[19] G.H. Dong, L.Z. Zhang, J. Phys. Chem. C 117 (2013) 4062–4068.
[20] G.G. Zhang, M.W. Zhang, X.X. Ye, X.Q. Qiu, S. Lin, X.C. Wang, Adv. Mater. 26 (2014) 805–809.
[21] G.H. Dong, Z.H. Ai, L.Z. Zhang, RSC Adv. 4 (2014) 5553–5560.
[22] Y. Zheng, L.H. Lin, X.J. Ye, F.S. Guo, X.C. Wang, Angew. Chem. Int. Ed. 53 (2014) 11926–11930.
[23] J.S. Zhang, M.W. Zhang, C. Yang, X.C. Wang, Adv. Mater. 26 (2014) 4121–4126.
[24] X.B. Chen, S.H. Shen, L.J. Guo, S.S. Mao, Chem. Rev. 110 (2010) 6503–6570.
[25] J. Gao, Y. Zhou, Z.S. Li, S.C. Yan, N.Y. Wang, Z.G. Zou, Nanoscale 4 (2012) 3687–3692.
[26] M. Tahir, C.B. Cao, N. Mahmood, F.K. Butt, A. Mahmood, F. Idrees, S. Hussain, M. Tanveer, Z. Ali, I. Aslam, ACS Appl. Mater. Interfaces 6 (2014) 1258–1265.
[27] G.H. Dong, L.Z. Zhang, J. Mater. Chem. 22 (2012) 1160–1166.
[28] J. Xu, Y.J. Wang, Y.F. Zhu, Langmuir 29 (2013) 10566–10572.
[29] J.H. Sun, J.S. Zhang, M.W. Zhang, A. Markus, X.Z. Fu, X.C. Wang, Nat. Commun. (2012) 1139–1146.
[30] P. Niu, L.L. Zhang, G. Liu, H.M. Cheng, Adv. Funct. Mater. 22 (2012) 4763–4771.
[31] H.X. Zhao, H.T. Yu, X. Quan, S. Chen, Y.B. Zhang, H.M. Zhao, H. Wang, Appl. Catal. B Environ. 152–153 (2014) 46–50.
[32] F. Dong, L.W. Wu, Y.J. Sun, M. Fu, Z.B. Wu, S.C. Lee, J. Mater. Chem. 21 (2011) 15171–15174.
[33] X.X. Zou, G.D. Li, Y.N. Wang, J. Zhao, C. Yan, M.Y. Guo, L. Li, J.S. Chen, Chem. Commun. 47 (2011) 1066–1068.
[34] M. Deifallah, P.F. McMillan, F. Corà, J. Phys. Chem. C 112 (2008) 5447–5453.
[35] K. Yohji, P. Robert, Ind. Eng. Chem. Fundam. 16 (1977) 163–169.